J. Fluid Mech. (2012), *vol.* 704, *pp.* 89–108. © Cambridge University Press 2012
doi:10.1017/jfm.2012.219

Finite-sample-size effects on convection in mushy layers

J.-Q. Zhong[1], A. T. Fragoso[1,3], A. J. Wells[1,2] and J. S. Wettlaufer[1,2,3,4]†

[1] Department of Geology and Geophysics, Yale University, New Haven, CT 06520, USA
[2] Program in Applied Mathematics, Yale University, New Haven, CT 06520, USA
[3] Department of Physics, Yale University, New Haven, CT 06520, USA
[4] NORDITA, Roslagstullsbacken 23, SE-10691 Stockholm, Sweden

(Received 4 January 2012; revised 30 March 2012; accepted 2 May 2012;
first published online 2 July 2012)

We report theoretical and experimental investigations of the flow instability responsible for mushy-layer convection with chimneys, drainage channels devoid of solid, during steady-state solidification of aqueous ammonium chloride. Under certain growth conditions a state of steady mushy-layer growth with no flow is unstable to the onset of convection, resulting in the formation of chimneys. We present regime diagrams to quantify the state of the flow as a function of the initial liquid concentration, the porous-medium Rayleigh number, and the sample width. For a given liquid concentration, increasing both the porous-medium Rayleigh number and the sample width drove a transition from a weakly convecting chimney free state to a state of mushy-layer convection with fully developed chimneys. Increasing the concentration ratio stabilized the system and suppressed the formation of chimneys. As the initial liquid concentration increased, onset of convection and formation of chimneys occurred at larger values of the porous-medium Rayleigh number, but the critical cell widths for chimney formation are far less sensitive to the liquid concentration. At the highest liquid concentration, the mushy-layer mode of convection did not occur in the experiment. The formation of multiple chimneys and the morphological transitions between these states are discussed. The experimental results are interpreted in terms of a previous theoretical analysis of finite amplitude convection with chimneys, with a single value of the mushy-layer permeability consistent with the liquid concentrations considered in this study.

Key words: buoyancy-driven instability, convection in porous media, solidification/melting

1. Introduction

The solidification of binary alloys and the formation of so-called mushy layers are important in applications across geophysics, geology and industry, ranging from sea ice growth (Feltham *et al.* 2006), to solidification in the Earth's interior (Bergman & Fearn 1994), to the formation of metal castings (Copley *et al.* 1970). Mushy layers are partially solidified reactive porous materials comprising solid crystals and interstitial melt, and formed as a result of morphological instability during the solidification of a two-component melt (Mullins & Sekerka 1964). An issue of significance in many applications is understanding the conditions for both the occurrence and the resulting

† Email address for correspondence: john.wettlaufer@yale.edu

https://doi.org/10.1017/jfm.2012.219 Published online by Cambridge University Press

dynamics of buoyancy-driven convection within the mushy region; see Worster (1997) for a review. Convective flow in a mushy layer transports fluid into regions of differing concentration, which can lead to local solidification or dissolution of the solid matrix and changes in the effective material properties. The permeability of the porous matrix depends on the local solid fraction, and hence flow focusing can accelerate the growth of the underlying convective-flow instability, and eventually lead to the formation of chimneys – channels of zero solid fraction that provide efficient pathways for buoyancy-driven flow out of the mushy layer. Understanding the onset and dynamics of convection in mushy layers with chimneys is of importance in geophysics for predicting brine fluxes from sea ice (Wettlaufer, Worster & Huppert 1997*b*; Wells, Wettlaufer & Orszag 2011), and in metallurgy because material heterogeneities associated with chimneys can lead to defects in metal castings (Copley *et al.* 1970).

Experimental studies of chimney formation in mushy-layer growth typically take one of two forms. Numerous so-called fixed-chill experiments have studied the transient growth of a mushy layer from a cold isothermal boundary and show that chimneys typically form after the mushy layer exceeds a critical thickness; see, for example, Aussillous *et al.* (2006), and references therein. As the thickness of the mushy layer continues to increase, it is observed that the mean spacing between chimneys also increases, with extinction of the flow in certain chimneys (Wettlaufer, Worster & Huppert 1997*a*; Solomon & Hartley 1998). Alternatively, one also considers steady-state mushy-layer growth. Directional solidification experiments, where the sample material is translated between two heat exchangers, indicate that multiple chimneys form for growth rates slower than a critical threshold that depends on the initial liquid concentration (Peppin, Huppert & Worster 2008; Whiteoak, Huppert & Worster 2008). Neufeld & Wettlaufer (2008*a*) used growth from a boundary with controlled time-dependent temperature in order to achieve steady-state growth and study the influence of an external shear flow on the onset of chimney formation. For both transient and steady-state growth the critical threshold for chimney convection can be interpreted in terms of an appropriate mushy layer Rayleigh number exceeding a critical value, so that buoyancy effects overcome dissipation and lead to the onset of convective fluid flow.

Theoretical modelling of convective flow in mushy layers has been approached from a variety of angles. Linear and weakly nonlinear stability analyses have considered the onset of convection during directional solidification under a wide variety of conditions; see, for example, Worster (1997), Guba & Worster (2010) and Roper, Davis & Voorhees (2011), and references therein for a review and more recent summaries. Several studies have revealed that the bifurcation to both steady and oscillatory convective flow states can be subcritical (Amberg & Homsy 1993; Anderson & Worster 1995; Guba & Worster 2006) depending on the growth conditions. Hence, this raises the possibility that finite amplitude perturbations may allow states with chimney convection to be accessed even when the base state of no flow is linearly stable. Convective states of finite amplitude have been considered either in direct simulations of particular growth conditions (Felicelli, Heinrich & Poirier 1998; Beckermann, Gu & Boettinger 2000; Guo & Beckermann 2003; Heinrich & Poirier 2004; Oertling & Watts 2004; Jain, Kumar & Dutta 2007; Katz & Worster 2008) or via studies of the system dynamics with an assumed periodic array of chimneys (Schulze & Worster 1998; Chung & Worster 2002; Wells, Wettlaufer & Orszag 2010). In a study of particular relevance here, Wells *et al.* (2010) used a numerical approach to consider the influence of changes in the spacing between chimneys on the evolution of system dynamics and the stability of solutions with steady-state chimney convection. This

https://doi.org/10.1017/jfm.2012.219 Published online by Cambridge University Press

approach demonstrates that the observed convective flow states are suppressed via a saddle-node bifurcation as the chimney spacing is reduced.

In this study we focus on the influence of a finite sample width on the formation of chimneys during mushy-layer convection. In § 2 we describe how the theoretical model of directional solidification of Wells *et al.* (2010) can be used to study the dynamics and stability of nonlinear convective flow states of finite amplitude. An experimental procedure is described in § 3 that produces steady-state mushy-layer growth for comparison to the theoretical predictions of Wells *et al.* (2010). An extensive set of experiments described in § 4 allows us to identify conditions for chimney formation for a variety of sample widths, growth rates and liquid concentrations, with comparison to the theoretical results providing an indirect estimate of mushy-layer permeability for several different liquid concentrations. We conclude with a discussion in § 5.

2. A model of mushy-layer convection with chimneys

A theoretical model of mushy-layer convection with chimneys was used by Wells *et al.* (2010) to investigate the dynamics of nonlinear convective flow, and is applied here to determine conditions under which flow states with a chimney can exist. We briefly summarize the essential features of the model below, noting that further details of the governing equations and boundary conditions are elaborated on in Wells *et al.* (2010). Furthermore, we emphasize here that whilst much of the motivation for this study involves subeutectic solidification from a cooled boundary above the solution, wherein the rejected solute (say salt) increases the density of the solution, here we are studying the solidification from below of a transeutectic solution, wherein the rejected 'solute' (say water) decreases the density of the solution, thereby driving upward buoyant convection.

2.1. *Physical and theoretical framework*

The model considers the directional solidification in two dimensions of a binary solution of local temperature T and local concentration C, translated at a speed V between hot and cold heat baths, as illustrated in figure 1. This results in a porous mushy region of thickness $h(x, t)$ bounded by an impermeable eutectic solid with temperature T_E and concentration C_E at $z = 0$, and an overlying fluid for $z > h$ with assumed uniform composition C_o and far-field temperature T_∞. We simulate flow with a chimney and single convection cell of width l, utilizing boundary conditions that simultaneously allow us to consider both convection cells that are either isolated, or in periodic arrays. The temperature T, local solid fraction ϕ and Darcy velocity $\boldsymbol{u}$ within the mushy region are calculated using time-dependent ideal mushy layer theory (Schulze & Worster 2005) which conserves heat and salt, accompanied by a condition of local thermodynamic equilibrium which couples the temperature and liquid concentration via a freezing point relationship $T = T_L(C)$. We use a linear approximation $T_L(C) \equiv T_E + \Gamma(C - C_E)$ for the freezing point relationship, where Γ is constant. Fluid velocities are determined from the incompressible Darcy flow law, where the permeability is assumed to be $\Pi = \Pi_0 (1 - \phi)^3$ for some reference permeability Π_0. We apply symmetry conditions on T and no normal flow at $x = l$, equivalent to either an insulating, impermeable boundary or a periodic array of convection cells.

The pure liquid flow in the narrow chimney is driven by buoyancy forces or pressure gradients and is parametrized using lubrication theory (see Wells *et al.* 2010, and references therein), where we apply symmetry conditions on the velocity $\boldsymbol{u}$ at $x = 0$.

https://doi.org/10.1017/jfm.2012.219 Published online by Cambridge University Press

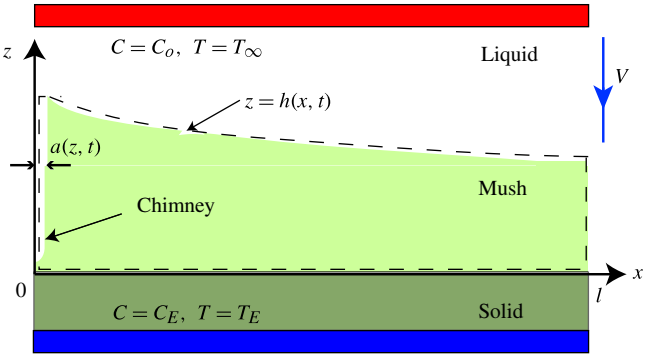


FIGURE 1. (Colour online) Schematic of the theoretical framework. Liquid of initial concentration C_o and temperature T_∞ is translated downward at speed V between hot and cold heat exchangers, and partially solidifies to form a mushy layer of thickness $h(x, t)$. We adopt a local co ordinate system (x, z) so that a eutectic solid of temperature T_E and concentration C_E forms at $z = 0$. We solve in a domain $0 \leqslant x \leqslant l$ and $0 \leqslant z \leqslant h(x, t)$ as indicated by the dashed outline, with a chimney of width $a(z, t)$ located at $x = 0$ in this domain. With suitable boundary conditions, described in the main text, this domain describes either a periodic array of convection cells separated by chimneys of width $2a(z, t)$ centred at $x = 0$ and with inter-chimney spacing $2l$, or else a single convection cell with chimney of width $a(z, t)$ against an impermeable free-slip vertical boundary.

This velocity boundary condition can describe either flow within two convection cells separated by a chimney of width $2a(z, t)$ centred at $x = 0$, or else a single convection cell with chimney of width $a(z, t)$ against an impermeable free-slip vertical boundary (a discussion of the likely influence of using a free-slip condition rather than a no-slip condition follows at the end of § 2.1). Combining the lubrication approximation with similar asymptotic approximations for heat transport yields nonlinear boundary conditions on the left-hand side of the mushy region, which is treated as a singular interface at $x = 0$. These conditions depend on the width of the chimney, with $a(z, t)$ updated to satisfy a condition of marginal equilibrium to just remove any constitutional supercooling. The boundary conditions at the mush–liquid interface and procedure for updating $h(x, t)$ are described in more detail in Wells *et al.* (2010). A pertinent point is that this approach uses a boundary layer approximation that describes the circulation and heat transport in the overlying fluid that is induced by the mushy-layer mode of convection, but neglects any component of buoyancy-driven convection that arises due to density differences within the overlying fluid region.

This model is characterized by six dimensionless parameters:

$$\left.\begin{aligned} \lambda = \frac{Vl}{\kappa}, \quad R_m = \frac{\rho_0 g \beta (C_0 - C_E) \Pi_0}{\mu V}, \quad \mathscr{C} = \frac{C_S - C_0}{C_0 - C_E}, \\ \theta_\infty = \frac{T_\infty - T_L(C_0)}{\Gamma (C_0 - C_E)}, \quad \mathscr{S} = \frac{L}{c_p \Gamma (C_0 - C_E)}, \quad Da = \frac{\Pi_0 V^2}{\kappa^2}, \end{aligned}\right\} \tag{2.1}$$

where the fluid density is approximated by $\rho_0[1 + \beta(C - C_E)]$ for constant haline coefficient β and reference density ρ_0, μ is the dynamic viscosity, g is the gravitational acceleration, κ is the thermal diffusivity, c_p is the specific heat capacity, L is the latent heat of fusion, and we have made the simplifying assumption that material properties are uniform in both solid and liquid phases, in line with ideal mushy layer theory (Schulze & Worster 2005). The numerical results presented herein investigate

https://doi.org/10.1017/jfm.2012.219 Published online by Cambridge University Press

how the dynamics change under variations of the dimensionless sample width λ and mush Rayleigh number R_m which characterizes the strength of buoyancy effects compared to dissipation. The experimental concentration and temperature conditions are reflected in the concentration ratio $\mathscr{C}$, θ_∞, and $\mathscr{S}$, with the Darcy number Da representing the relative permeability of the porous matrix. For example, an increase in liquid concentration C_0 leads to the values of the concentration ratio $\mathscr{C}$, the Stefan number $\mathscr{S}$, and the dimensionless liquid temperature θ_∞ all being reduced. Changes in these parameters influence the stability of mushy layers in different ways (Worster 1992). Thus, if $\mathscr{C}$ is reduced, then the mean solid fraction is higher and hence the local permeability is reduced within the interior of the mush. Additionally, a reduced value of $\mathscr{C}$ leads to a thinner mushy layer and reduces the potential energy that is available to drive flow. Hence, both of these effects act to stabilize the system. In contrast, a smaller value of $\mathscr{S}$ implies a reduced influence of latent heat, enhancing the dissolution of crystals. Finally, reduction of θ_∞ reduces the heat flux from the liquid, allowing the mushy layer to grow thicker, thereby providing greater potential energy to drive flow. These latter two effects promote growth of the instability.

It is difficult to directly constrain and measure the permeability in experimental settings, and so in § 4.2 we determine a reference value of $\Pi_0 = 1.6 \times 10^{-5}$ cm^2 for a range of liquid concentrations, by comparison between experimental data and theoretical prediction. This provides an indirect estimate of the permeability for solidification in a Hele-Shaw cell. Comparison to other estimates in different settings will be discussed in § 5. Importantly, we note that an independent set of simulations that vary Da with all other parameters held fixed show that whilst the chimney width varies with scaling $aV/\kappa \sim Da^{1/3}$, consistent with the scaling analysis of Schulze & Worster (1998), the fluid flux remains constant at leading order over the range $10^{-4} \leqslant Da \leqslant 5 \times 10^{-3}$. The same features have also been observed in a recently developed simplified model of convection in mushy layers (Rees-Jones & Worster, personal communication). This behaviour is consistent with the flow dynamics being controlled by buoyancy-driven flow within the mushy region, whilst the chimney width adjusts passively to accommodate the necessary liquid flux. Hence, the mushy region flow dynamics do not depend strongly on the ratio of flow resistance in the porous mushy region to viscous resistance in the liquid region, consistent with only a weak dependence on Da. We maintain the value $Da = 5 \times 10^{-3}$ throughout all numerical results reported here.

The fact that flow in the mushy region is relatively insensitive to viscous resistance in the liquid region also suggests that qualitatively similar results would be obtained by application of a free-slip and a no-slip boundary condition in the chimney. The boundary condition describing flow at the chimney edge takes the form

$$\psi = \alpha_1 \frac{R_m}{Da}\left(\frac{aV}{\kappa}\right)^3 \kappa V\left[\frac{1}{3R_m\,(1-\phi)^3}\frac{\partial \psi}{\partial x} + \frac{3\alpha_2}{20}V\frac{C-C_E}{C_0-C_E}\right] + \alpha_3 a\frac{\partial \psi}{\partial x}, \qquad (2.2)$$

(Wells *et al.* 2010), where the streamfunction ψ satisfies $\boldsymbol{u} = (-\psi_z, \psi_x)$ and the constant pre-factors are $\alpha_1 = \alpha_2 = \alpha_3 = 1$ for a free-slip boundary, or $\alpha_1 = 1/4$, $\alpha_2 = 2/3$ and $\alpha_3 = 1/2$ for a no-slip boundary. For fully developed chimneys, with $aV/\kappa \sim Da^{1/3}$, the final term on the right-hand side of (2.2) is $O(Da^{1/3})$ smaller than the remaining terms (Schulze & Worster 1998), and so an order-one change in α_3 does not impact the leading-order behaviour. Next, we note that the numerical coefficient of the buoyancy term (featuring α_2) has been determined using a Polhausen approximation in the current calculations (Wells *et al.* 2010). Previous calculations

https://doi.org/10.1017/jfm.2012.219 Published online by Cambridge University Press

using a different form of approximation yield a different numerical coefficient, but qualitatively similar mushy region flow dynamics (Chung & Worster 2002). Hence, we expect an order-one change in α_2 to also produce qualitatively similar dynamics. Finally, the difference in α_1 between free-slip and no-slip boundaries can be compensated for by a rescaling of the Darcy number $Da \to 4Da$. Hence, because the flow in the mushy layer is insensitive to Da at leading order, we expect no qualitative difference in the leading-order dynamics within the mushy region between cases with a free-slip or a no-slip boundary condition in the chimney.

2.2. *Numerical method*

The solution procedure combines two different numerical approaches involving both time-dependent calculations, and an arclength-continuation scheme. The time-dependent simulations combine second-order finite differences in space, with semi-implicit Crank–Nicolson time-stepping, and free boundaries updated via relaxation (see Wells *et al.* 2010 for further details). The resulting systems for temperature and streamfunction were solved using a multigrid iterative method (Adams 1989; Briggs, Henson & McCormick 2000). This time-dependent code was complemented by an arclength-continuation method (Keller 1977) that traces both stable and unstable solution branches, allowing us to verify that the relaxation procedures do not have a strong influence on the stability of the system. In order to reduce the computational costs in solving the systems involving Jacobian terms that are required for arclength continuation, the predictor–corrector calculations are computed from projections of the finite difference solutions onto a basis of products of Chebyshev polynomials in x and y. This allows the main characteristics of the solution to be characterized by a smaller number of degrees of freedom. The resulting solutions predicted by arclength continuation in Chebyshev space are then refined using a steady version of the finite-difference code.

2.3. *Stability boundaries*

In this paper we are interested in the influence of sample width on the formation of chimneys in a mushy layer. To determine conditions for the existence of states with chimneys, the arclength-continuation method is used to trace solution branches as λ varies with R_m, $\mathscr{C}$, $\mathscr{S}$, θ_∞ and Da all held fixed, applying the method of Wells *et al.* (2010) to a region of parameter space relevant to our experiments. Figure 2 shows a typical example of the system evolution, where F is the dimensionless solute flux from the chimney. Two steady states are observed, an upper branch of chimney convection (solid curve) and a lower branch of no flow (triangles), along with an intermediate unstable branch of chimney convection (dashed curve). Starting on the upper branch of stable chimney convection, as λ is decreased the system undergoes a saddle-node bifurcation at $\lambda = \lambda_c$ so that the chimney convection state ceases to exist for $\lambda < \lambda_c$. Having determined the critical wavelength λ_c, the above procedure is repeated with varying R_m but $\mathscr{C}$, $\mathscr{S}$, θ_∞ and Da held fixed to obtain a stability boundary of the form $\lambda = \lambda_c(R_m)$. Examples of such stability boundaries and their comparison to experimental data are shown later in figure 7 and discussed in § 4. Note that, by construction, the theory predicts that flow with a single chimney at the centre of two symmetric convection cells requires twice the domain width as the corresponding state with a single convection cell and chimney at the sidewall. Hence one intuitively expects that a state of convection with a single chimney at the wall can be achieved at smaller Rayleigh numbers and narrower cell widths than convection with chimneys away from the sample walls.

https://doi.org/10.1017/jfm.2012.219 Published online by Cambridge University Press

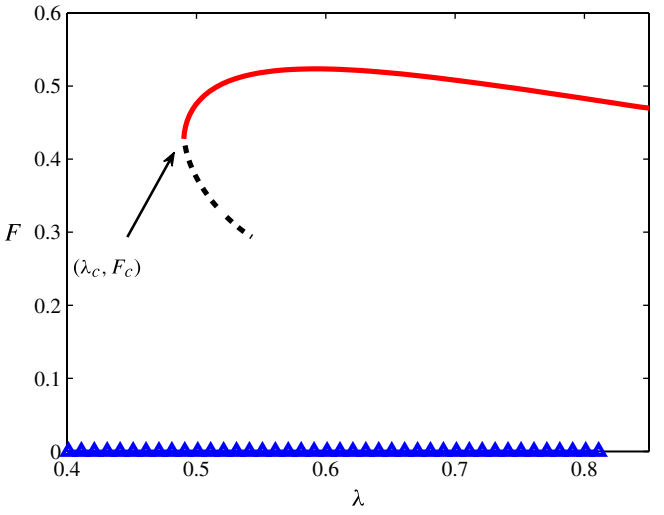


FIGURE 2. (Colour online) Variation of the calculated dimensionless brine flux F with convection cell width λ for steady-state flow with $R_m = 32.5, \mathscr{C} = 11.7, \mathscr{S} = 4.8, \theta_\infty = 0.185$, and $Da = 0.005$, consistent with solidification of a 27 wt% aqueous ammonium chloride solution described in § 3. The system shows hysteresis, with multiple stable steady states. The stable upper branch of chimney convection (solid curve) and stable lower branch of no flow (triangles), are accompanied by an intermediate unstable branch of chimney convection (dashed curve). The system undergoes a saddle-node bifurcation at (λ_c, F_c), with the stable state of chimney convection ceasing to exist for $\lambda < \lambda_c$. Failure of convergence of the iterative corrector scheme prevents further continuation along the unstable branch.

3. Experimental apparatus and methods

3.1. *Experimental apparatus*

A schematic diagram of the apparatus is shown in figure 3(*a*). A Hele-Shaw sample container, A, of inner dimensions 25.40 cm × 15.24 cm × 0.32 cm is surrounded by an air-flow vessel, B. The container walls, C, are made of 0.8 cm thick, optically clear Plexiglas, and extend 0.6 cm below the top surface of the bottom plate, D. The seal which confines the working fluid is provided by high-strength silicon adhesive (RTV 732) below the walls. Spacers, E, made by low-thermal-conductivity Plexiglas divide the container into a subset of cells with adjustable width l. The width of the spacers $l_s = 1.3$ cm is chosen to provide sufficient thermal insulation between the convection cells. The thermal diffusion time over the spacers, l_s^2/κ_s, is of the order of hours (κ_s is the thermal diffusivity of Plexiglas), and is comparable to the whole time span of the solidification process. In this manner, mushy layers grow in each of the convection cells independently, and each is subjected to spatially uniform cooling from the bottom plate.

The cell bottom, D, is made from a 1.3 cm thick high-thermal-conductivity copper plate. Three thermistors are embedded in D with a 0.3 cm distance to the top plate surface (shown by the solid black circles in figure 3*a*). These monitor the bottom temperature of the sample which, as discussed in § 3.2, is in general controlled to be time-dependent with $T_B = T_B(t)$. Except where we want to emphasize the time-dependence, for parsimony of notation in what follows we simply write T_B. To inhibit chemical reactions with the working fluid, the top surface of D is painted with a 0.1 mm thick layer of anti-corrosion coating (PRO 15). When the highest thermal

https://doi.org/10.1017/jfm.2012.219 Published online by Cambridge University Press

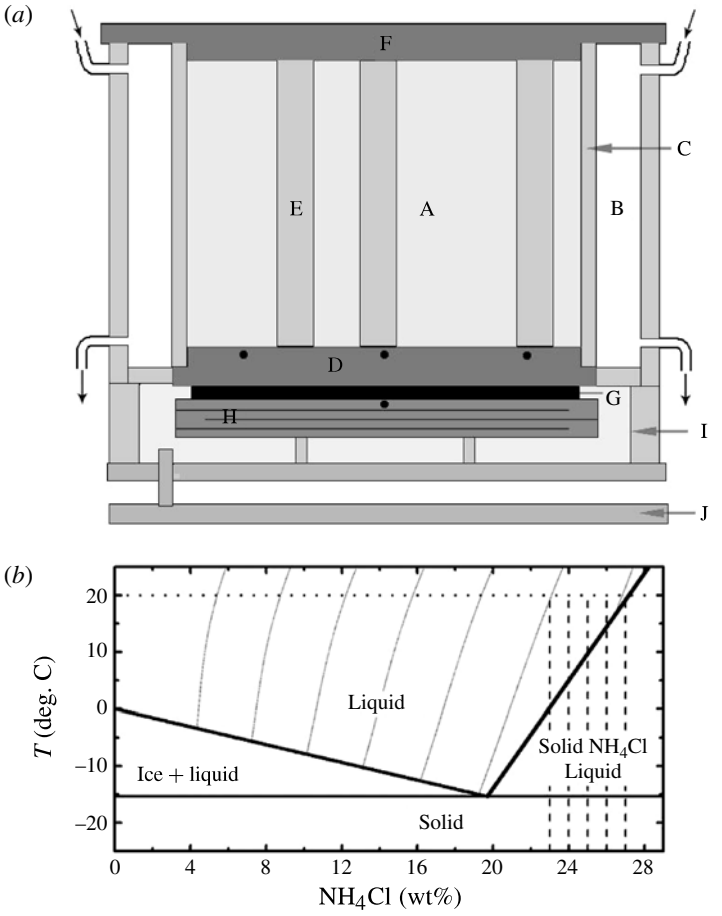


FIGURE 3. (*a*) Schematic of the experiment apparatus. See text in § 3.1 for detailed identification of the various components. (*b*) Phase diagram of the NH_4Cl–H_2O solution. The horizontal dotted line shows the far-field temperature T_∞ and the vertical dashed lines indicate the initial liquid concentrations chosen in the experiment. The corresponding liquidus temperatures $T_L(C_0)$ are given by the intersection of each dashed line with the solid liquidus curve. Solution density isopleths are indicated by the faint lines with positive slope above the liquidus and were constructed using data from the US National Research Council (2003). Note that in our study the rejected material is depleted in salt and thus has a lower density than the solution, thereby driving upward buoyant convection.

flux is applied through the sample, this coating is responsible for a temperature difference of 0.3 K between T_B and the fluid temperature measured at the bottom of the sample. Corrections have thus been made for T_B to accurately reflect the bottom fluid temperature.

The sample cell is enclosed by an air-flow vessel, B. Ambient air enters and leaves through outlets in this vessel, as indicated by the arrow heads in figure 3(*a*), at a rate of approximately 50 $cm^3\ s^{-1}$. The air flow has been thermally stabilized at $T_\infty = 20 \pm 0.2$ °C in a large reservoir before entering the vessel to provide a steady thermal environment. Simultaneously, we flow dry air flow through this region to suppress water condensation on the sample walls, C, during the solidification process. An aluminium top plate, F, maintains a constant far-field temperature T_∞ of the

https://doi.org/10.1017/jfm.2012.219 Published online by Cambridge University Press

sample. The working fluid confined in the cell is an aqueous NH_4Cl solution with initial concentration C_0. The density and temperature of the solution are measured before the experiments using a oscillating-type densitometer (Antor Paar, DMA 35N). The concentration C_0 is then chosen between 23 and 27 wt% with an accuracy better than ± 0.1 wt% using the isopycnal lines as shown in the phase diagram in figure 3(*b*).

In thin cells the thermal boundary conditions of the sample may be affected by heat flow through the walls to the working fluid, which has been considered explicitly in a recent mathematical model (Peppin *et al.* 2007). Because of the finite thermal resistance of the wall material, a sample cell with wall temperature profiles that match entirely the fluid temperature is necessary to eliminate the lateral heat flow effects. The double-sided wall construction in the present experimental system effectively minimizes this heat loss effect. For a quantitative evaluation of the lateral heat lost through the sidewalls, we measure the fluid temperatures by moving a temperature probe along the shortest dimension of the cell, at a horizontal level 3 mm above the mush–liquid interface before the formation of the chimneys. The temperature variation is within 0.03 K over the full thickness (0.32 mm) of the cell, with the centre fluid temperature slightly higher than that near the sidewalls. Thus, we conclude that the vertical heat flux through the sample dominates the lateral heat lost along the sidewalls, and that the temperature field in the liquid region is essentially two-dimensional.

Underneath the bottom of the sample cell there is an array of Peltier devices, G (thermoelectric coolers), sandwiched between the copper plate, D, and a 2.5 cm thick copper manifold, H. The temperature of the manifold is regulated through the circulation of anti-freezing coolant. High-conductivity thermal compound is pasted between the Peltier devices and the copper plates to enhance the thermal contacts and improve the thermal homogeneity on the bottom plate of the sample. Under typical experimental conditions, the horizontal temperature heterogeneity along the sample bottom is within 0.05 K, as measured by the three thermistors embedded in part D.

Supporting the copper manifold, H, a thermal insulating based shield, I, rests on a levelling plate, J, through which the entire apparatus can be levelled within 0.005 rad.

3.2. *Thermometry and thermal control protocol*

The bottom-plate temperature T_B and top-plate temperature T_∞ are measured with thermistors embedded in the bottom plate D and the top plate F. The fluid temperature in the liquid region is measured by thermistors inserted inside the sample through 0.6 mm diameter stainless steel tubing. All thermistors are calibrated to a precision of 1 mK against a Hart Scientific model 5626 platinum resistance thermometer and are traceable to the ITS-90 temperature scale. Consistency between the thermistors is within 0.01 K.

Recent experiments (Peppin *et al.* 2007, 2008) investigated steady-state mushy-layer growth using an experimental apparatus in which the solution is translated at prescribed rates between two heat exchangers. In the present experiment, steady growth is accomplished by time-dependent temperature control as $T_B(t) = T_B^\circ - \gamma t$, where γ is the constant cooling rate. This form was chosen because Neufeld & Wettlaufer (2008*a*) found that a linear approximation of their equation (4.6) was empirically realized over an experimentally relevant time interval as seen in their figure 9(*b*). Indeed, as seen in figure 4, this is also true for our cell configuration and its relatively small volumes.

Following the protocol developed in a recent experimental study, control of the sample bottom-plate temperature $T_B(t)$ is achieved by two cooling mechanisms (Neufeld & Wettlaufer 2008*a*). First, we use an array of Peltier devices (part G in figure 3*a*) to produce a thermal flux from the bottom plate D. The downward heat flux, which is proportional to the applied electrical power to the Peltier devices, is

https://doi.org/10.1017/jfm.2012.219 Published online by Cambridge University Press

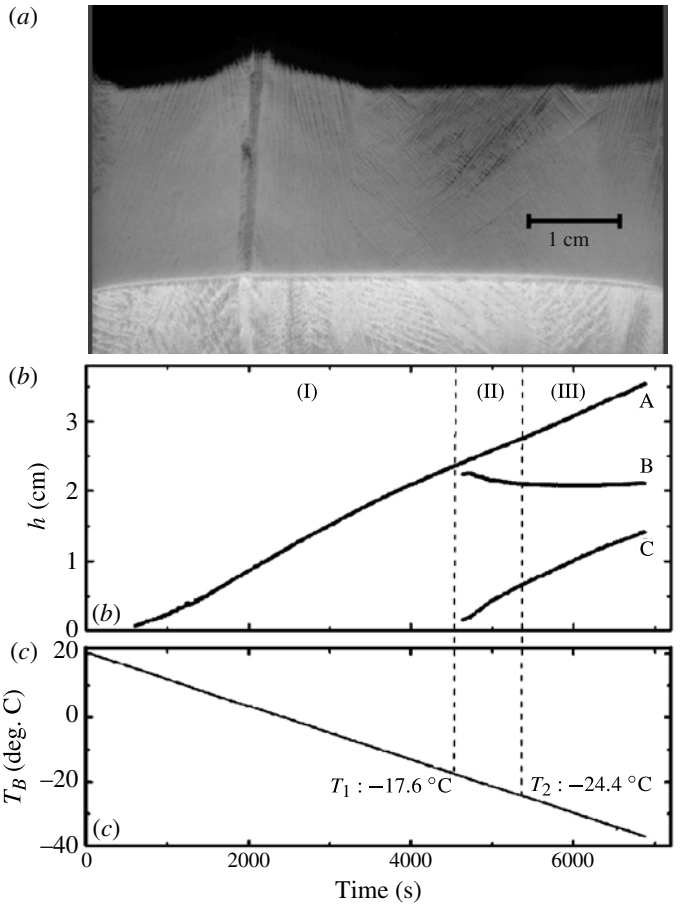


FIGURE 4. (*a*) Image of a mushy layer growing from a 27 wt% NH_4Cl solution under a cooling rate of $\gamma = 0.5$ K min^{-1}. The bright white curve is the eutectic–mush interface. The horizontal black bar is 1 cm. (*b*) Time-recording of the mushy-layer thickness depicting three growth periods. Curve A, height H_I of the mush–liquid interface; curve C, height H_E of the eutectic solid layer; curve B, thickness of the mushy layer $h \equiv H_I - H_E$. (I) Linear-growth period during which the bottom-plate temperature T_B is above the eutectic temperature T_E. The mushy layer grows linearly with time until the eutectic solid forms. (II) The initial transient-growth period ($T_1 > T_B > T_2$) during which the eutectic layer starts to grow. The mushy-layer thickness depends on time but finally converges to a constant. (III) Steady-growth period ($T_B < T_2$). The mushy-layer thickness remains constant. (*c*) The linearly decreasing bottom-plate temperature T_B. The two dashed lines in (*b*) and (*c*) show the two temperatures at the transitions between states: $T_1 = -17.6$ °C and $T_2 = -24.4$ °C.

controlled in a feedback loop that incorporates the instantaneous temperature readings for T_B, and is delivered to the Peltier devices by a programmable power supply (Sorenson, Model DCS 40-25). A second ingredient of the cooling-control settings is the coolant-circulating copper manifold, H. Anti-freeze coolant is circulated in a double-spiral channel built inside manifold H, driven by two Neslab (RTE-7) baths at a flow rate of 500 cm^3 s^{-1} and a cooling capacity of 1000 W at 20 °C. The bath-temperature stability achieved over long time scales is within 0.01 °C, as measured by the thermistor embedded in the manifold H. The Peltier devices provide fast control of

https://doi.org/10.1017/jfm.2012.219 Published online by Cambridge University Press

the temperature variation on the bottom plate D. During the experiment a prescribed linearly decreasing bottom-plate temperature T_B of the sample is maintained down to approximately -40 °C (figure 4*c*), which forces steady growth of the overlying mushy layer as depicted in figure 4(*b*).

4. Results

4.1. *Steady-state mushy-layer growth*

One representative set of data for the mushy-layer growth as a function of time is shown in figure 4(*b*). There are three distinct periods, with different characteristic variations of $h(t)$ with time. To the left of the first dashed line at $T_B = T_1 = -17.6$ °C (shown in figure 4*c*), the thickness of the mushy layer increases linearly with a growth speed of 6.60 μm s^{-1}. No eutectic layer is formed in this period. Formation of a eutectic solid layer underlying the mushy layer starts at $T_B = T_1$. As the bottom-plate temperature T_B further decreases, an initial transient-growth period appears between (-17.6 °C, -24.4 °C), as indicated by the two vertical dashed lines. Growth of the mushy layer in this period is dependent on initial conditions, particularly the cooling history before T_B reaches T_1.

To the right of the second dashed line at $T_B = T_1 = -24.4$ °C, both the advancing speed of the mush–liquid interface, $\dot{H}_I$, and the eutectic–mush interface, $\dot{H}_E$, are constant and equal $V = 4.86$ μm s^{-1}. The thickness of the mushy layer, $h = H_I - H_E$, thus remains a constant independent of the initial cooling process. The thickness of both the mushy layer and the eutectic layer in this steady-growth period are shown in figure 4(*a*).

From the description above it is clear that the advancing speed of the mush–liquid interface V is not a prescribed control parameter in this study but depends on the bottom-plate cooling rate γ and the initial liquid concentration C_0. In figure 5(*a*) we show that at high cooling rates, when $\gamma > 1.0$ K min^{-1}, V increases with C_0, whereas at low cooling rates $\gamma \leqslant 1.0$ K min^{-1}, V is nearly independent of C_0.

In figure 5(*b*) we show data for the mushy-layer thickness h during a steady state of chimney convection at cooling rates covering 0.5 K $min^{-1} \leqslant \gamma \leqslant 2.5$ K min^{-1}. The dependence of h as a function of the bottom-plate temperature is shown in the inset for three cooling rates $\gamma = 0.5$, 1.0 and 2.5 K min^{-1}. When T_B is sufficiently low the system easily reaches a steady state. The mushy-layer thickness h is then evaluated when it converges to a constant and is independent of T_B. Figure 5(*b*) shows that the mushy layer tends to be thicker at lower γ, leading to a higher mushy-layer Rayleigh number. These trends agree qualitatively with theoretical predictions (Worster 1992).

Results for h at the same cooling rates γ are repeatable from run to run and are independent of the pre-cooling process. The inter-experimental variation of the steady-state mushy-layer thickness h is within 5 %, as indicated by the error bars in figure 5(*b*). Experiments with very low cooling rate $\gamma < 0.5$ K min^{-1} show that the advancing speed of the eutectic–mush interface is always larger than that of the mush–liquid interface ($\dot{H}_E > \dot{H}_I$), leading to a decreasing mushy-layer thickness, and the system does not reach a steady state within the experimental time frame. Due to the finite cooling capacity of the experimental apparatus, at experiments with high cooling rate $\gamma > 2.5$ K min^{-1}, the bottom-plate temperature T_B deviates from the usual linearly decreasing trends in the low-temperature range. Data analysis in these experiments is limited by the shorter period of growth.

https://doi.org/10.1017/jfm.2012.219 Published online by Cambridge University Press

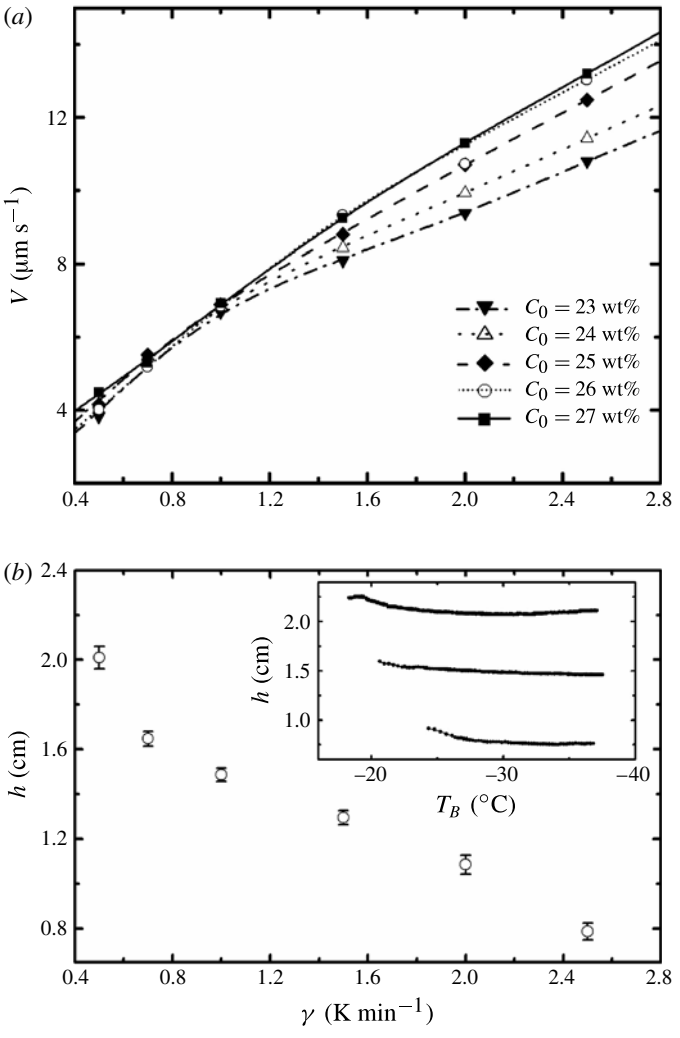


FIGURE 5. (*a*) Growth velocity V of the mush–liquid interface as a function of the cooling rate γ in a steady-growth state with $l = 2.54$ cm. The solid and dashed lines denote spline fits for each set of data points. The legend denotes the initial concentrations for each curve. (*b*) Height of the mushy layer h as a function of the cooling rate γ in a steady-growth state with $C_0 = 27$ wt%, $l = 2.54$ cm. The error bars indicate the variation in h for different runs under the same experimental conditions. Inset: The mushy-layer height h as a function of T_B at three cooling rates. From top to bottom, the three curves show data for $\gamma = 0.5$ K min^{-1}, $\gamma = 1.0$ K min^{-1} and $\gamma = 2.5$ K min^{-1}, respectively.

4.2. *Instability and onset of mushy-layer convection with chimneys*

For a given liquid concentration C_0, an increase of the Rayleigh number above a critical value R_m^c, or of the cell width $\lambda = Vl/\kappa$, led to a transition from a weakly convecting chimney free state to a state of mushy-layer convection with fully developed chimneys as seen in figure 4(*a*). The transition from the no-chimney state to the state of mushy-layer convection with chimneys depends on the liquid concentration C_0 through $\mathscr{C}$, $\mathscr{S}$ and θ_∞. We ascribe the experimental transition at

https://doi.org/10.1017/jfm.2012.219 Published online by Cambridge University Press

a critical Rayleigh number R_m^c to the saddle-node bifurcation at $\lambda = \lambda_c$ and $F = F_c$ described in figure 2. To identify a convective state in which chimneys form, we capture shadowgraph images to illustrate two-dimensional fluid density variations for visualization of compositional plumes emerging from the mushy layer. We require a state of chimney convection to satisfy three criteria. First, there is a channel of zero solid fraction within the mushy region (figure 4*a*). Second, there is at least one vigorous compositional plume in the far-field liquid region. Since intermittent chimney plumes (or convection in a breathing mode: Solomon & Hartley 1998; Peppin *et al.* 2008) are commonly observed in the experiment, we consider a chimney plume if its lifetime is longer than the diffusion time scale for boundary layer convection $d^2/D \sim 10$ min. Here $d \sim 1$ mm is the average size of an isolated plume detached from the compositional boundary layer in the liquid region and D is the solute diffusivity. Third, other turbulent buoyant plumes in the near field next to the chimney plume have become substantially diminished, which indicates suppressed boundary-layer-mode convection in concert with the formation of the chimney. Transition from a state of no flow to a state of chimney convection is readily identified through shadowgraph pictures. In figure 6, we see the flow patterns in the liquid region when two sets of parameters (λ, R_m) are chosen. Figure 6(*a*) shows that in a stable state of no flow (these data points are indicated by upward triangles in figure 7*b*), there is no chimney flow in the far field of the liquid region in any of the cells, while small-scale turbulent plumes driven by the boundary-layer-mode convection remain active. When the value of R_m increases slightly (indicated by downward triangles in figure 7*b*), chimney flow penetrates into the far field in the two largest cells (figure 6*b*), which are readily discernible from the small-scale turbulent plumes and dominate the flow field in the liquid region. We thus conclude that the mushy layers growing in the two largest cells are both in an unstable configuration that leads to a state of chimney convection.

We determine the pre-factor of the permeability of the mushy layer Π_0 in the following manner. By adjusting a single value of Π_0 that is the same for three different liquid concentrations, we determine values of R_m from the experimental data so that the boundary between the stable and unstable regimes is closest to the stability curve derived from numerical calculations. As illustrated in figure 7, the resulting comparison with the theoretical curves is consistent with the observed stability to within one increment in cell width λ. Hence, this comparison between theory and experiment allows us to empirically estimate the permeability as $\Pi_0 = 1.6 \times 10^{-5}$ cm^2, independent of liquid concentration in the range 24 wt% $\leqslant C_0 \leqslant$ 27 wt%. One can thus interpret this procedure as adjusting the pre-factor Π_0 in the permeability function $\Pi(\phi) = \Pi_0 (1-\phi)^3$ so that the model results with this form of permeability agree best with experiment. Whilst we realize there are other possible choices of permeability function, and we discuss this issue in § 5, this permeability relationship captures variation in $\Pi(\phi)$ between the two end members of $\phi = 0$ at the mush–liquid interface and $\phi \sim 1$ in the solid. Because our experimental measurements examine only bulk features of the flow, we cannot justify a detailed comparison of different functional forms for $\Pi(\phi)$.

As seen in figure 7(*a*), mushy-layer growth at a low initial liquid concentration ($C_0 = 24$ wt%) is mostly stable. Chimneys are present only at high values of R_m and large λ. Figure 7(*b*) shows that as the liquid concentration increases (to $C_0 = 25$ wt%), the critical R_m^c decreases. Moreover, the sensitivity of R_m^c to λ increases, abruptly increasing as the confinement increases (i.e. as λ decreases) and preventing the onset of mushy-layer mode convection. When the liquid concentration further increases to

https://doi.org/10.1017/jfm.2012.219 Published online by Cambridge University Press

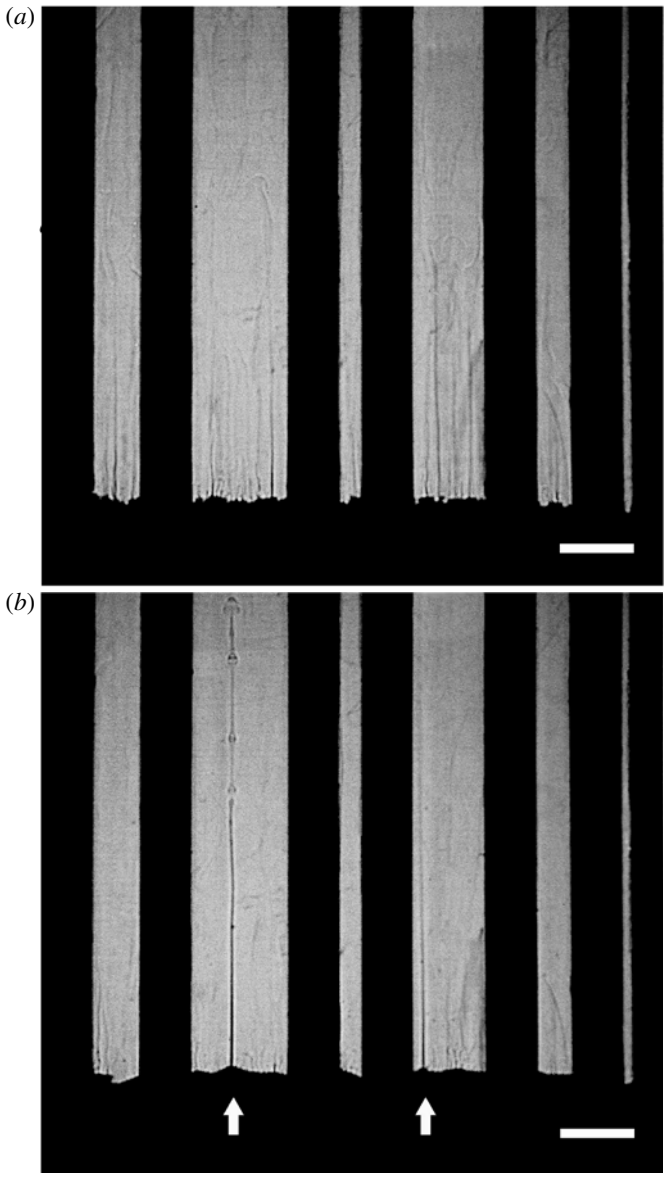


FIGURE 6. Shadowgraph images captured for $C_0 = 25$ wt% and (*a*) $\gamma = 1.5\ \mathrm{K\ min^{-1}}$, (*b*) $\gamma = 1.0\ \mathrm{K\ min^{-1}}$. Stability analysis results based on such images are presented in the regime diagrams in figure 7(*b*) by downward and upward triangles, respectively. Both pictures are taken at $T_B = -40.0\ ^\circ\mathrm{C}$. Note the formation of a strong chimney plume in each of the two largest cells in (*b*), indicated by two white arrows. The horizontal white bars show 2 cm. On the time scale of the experiments we could not measure any changes in the far-field concentration C_0.

$C_0 = 27$ wt%, solidification of the sample with large λ becomes unstable for all the values of R_m obtained from the experiments as shown in figure 7(*c*). In summary, the system becomes less stable as the liquid concentration C_0 increases, which can be interpreted as follows. An increase in liquid concentration C_0 leads to the values of the

https://doi.org/10.1017/jfm.2012.219 Published online by Cambridge University Press

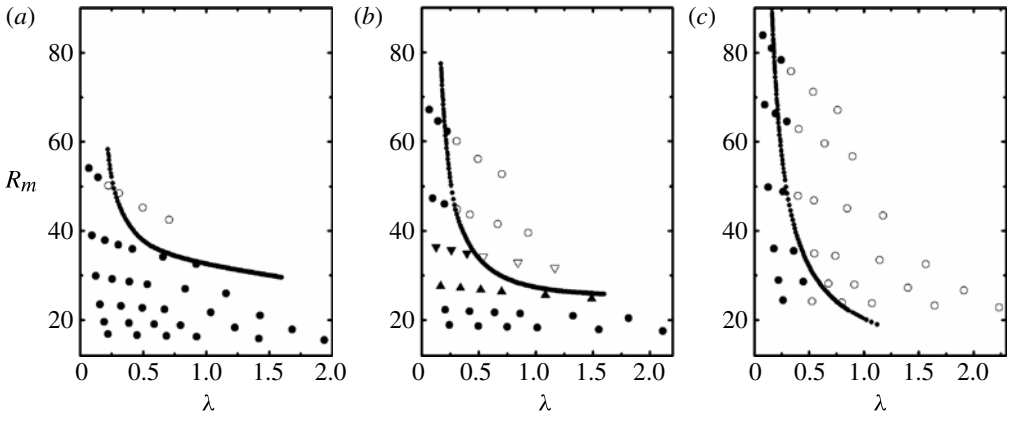


FIGURE 7. Regime diagrams depicting the onset of mushy-layer convection with chimneys. Solid symbols, mushy layer grows in a stable state; open symbols, unstable state with formation of at least one chimney within the mushy layer. (*a*) Results for $C_0 = 24$ wt%. (*b*) Results for $C_0 = 25$ wt%. The triangles indicate the experimental results illustrated by shadowgraph pictures in figure 6. (*c*) Results for $C_0 = 27$ wt%. Similar experiments for $C_0 = 23$ wt% (not shown) resulted in no chimney formation for this range of cell widths and Rayleigh numbers. Experimental values of the Rayleigh number are calculated using the reference permeability $\Pi_0 = 1.6 \times 10^{-5}$ cm^2 for all three liquid concentrations, determined as described in the main text. Black curves: numerical results for the stability curve indicating the critical R_m^c as a function of λ.

concentration ratio $\mathscr{C}$, the Stefan number $\mathscr{S}$, and the dimensionless liquid temperature θ_∞ all being reduced. Changes in these parameters influence the stability of the system in different ways, as identified in the linear stability analysis of Worster (1992). If $\mathscr{C}$ is reduced, then the mean solid fraction is higher and hence the local permeability is reduced within the interior of the mush. In addition, a reduced value of $\mathscr{C}$ leads to a thinner mushy layer and reduces the potential energy that is available to drive flow. Both of these effects make the system more stable. A smaller value of $\mathscr{S}$ implies that the influence of latent heat is smaller, so that the solid matrix is dissolved more easily. This promotes growth of the instability. A smaller value of θ_∞ leads to a smaller heat flux from the liquid, so that the mushy layer grows thicker and provides greater potential energy to drive flow. The present theoretical simulations of finite amplitude convection reveal that the net combination of these competing effects results in the system becoming less stable as the liquid concentration C_0 is increased.

4.3. *Variability, multiple chimneys and morphological transitions between states*

Depending on the growth speed of the mushy layer and the size of the sample cell, several morphological transitions are observed in the states displaying chimney convection. To illustrate these morphological transitions we present these results as regime diagrams for three repetitions of experiments with $C_0 = 27$ wt% in figure 8. The comparison between the three repetitions in figures 8(*a*), 8(*b*) and 8(*c*) is indicative of the role of fluctuations in influencing different experimental realizations. The stability boundary between states with and without flow is robust to within inter-experimental variation of one increment amongst the set of cell widths. The variability between observed states with and without flow under the same experimental conditions might be explained in part by the theoretically suggested subcritical

https://doi.org/10.1017/jfm.2012.219 Published online by Cambridge University Press

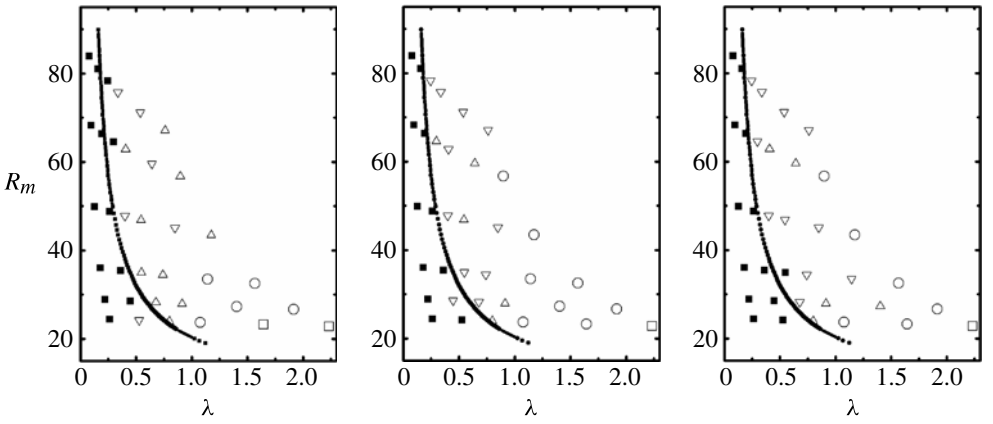


FIGURE 8. Regime diagrams depicting the onset of mushy layer convection with chimneys. Data obtained from three sets of experiments with $C_0 = 27$ wt%. Solid squares, stable state, mushy layer with no chimney; open down-triangles, one chimney forms at the walls; open up-triangles, one chimney forms off the walls; open circles, formation of two chimneys within the mushy layer; open squares, formation of three or more chimneys within the mushy layer; black curves, numerical results for the stability curve indicating the critical R_m^c as a function of λ (corresponding to a single convection cell with a chimney at the wall).

instability behaviour: the form of perturbation required to trigger a transition to a finite amplitude convecting state might only be achieved in a subset of the experiments. The variability may also be influenced by factors not described in the theory, such as weak heat loss through the walls or boundary-layer-mode convection.

The regime diagrams in figure 8 also reveal a preference for chimney formation at the cell walls when the system undergoes a transition from a state of no flow to a state of chimney convection at $\lambda \equiv \lambda_{c,1}$. Combining all the data in figure 8, for each cooling rate we determine the states at the smallest sample width that permits convection. Using this method we find four cell widths where a single chimney is observed at the cell wall, and the remaining two cell widths show either a chimney at the wall, or a chimney in the sample interior, for different repetitions under the same conditions. Localization of the mushy-layer mode of convection near the walls has been observed in both experiments and models (Giamei & Kear 1970; Felicelli *et al.* 1998). Recent theoretical calculations show that chimney formation can be influenced by lateral heat transfer due to heat losses at the sidewalls. Sidewall heat transfer can have both direct thermal effects and indirect effects, by forming weak convective flows in the overlying fluid (Roper, Davis & Voorhees 2007; Roper *et al.* 2011). The cooling effect of sidewall heat losses can promote the formation of chimneys near to the walls (Roper *et al.* 2007). Whilst localization of convection resulting from flow in the overlying fluid encourages chimney formation at the walls in three-dimensional mushy layer cells, in two-dimensional flow the localization promotes chimney formation away from the cell walls. Hence, this form of flow localization cannot be the controlling factor in our quasi-two-dimensional Hele-Shaw cell. As an alternative factor, our theoretical model suggests that the preference for wall chimneys close to the critical cell width for onset of convection may simply be a geometrical effect due to the finite-sample-width effects in our experiment. If the stability boundary $\lambda = \lambda_{c,1}$ for states with one chimney at the wall is interpreted as the minimum width of a single convection cell, then the narrowest sample widths that can support convection

https://doi.org/10.1017/jfm.2012.219 Published online by Cambridge University Press

necessarily have a chimney at the wall. A state with a central chimney separating two symmetric convection cells requires a minimum cell width $\lambda = 2\lambda_{c,1}$. Whilst we have not conducted detailed stability calculations for asymmetric states where an interior chimney is located away from the centre of the sample, it is plausible that certain forms of these states might be stable over the range $\lambda_{c,1} < \lambda < 2\lambda_{c,1}$, with the chimney separating a dominant convection cell of width greater than $\lambda_{c,1}$ from a narrower passive region. The possibility of asymmetric arrangements of convection cells is also likely to be of relevance in describing the observed transitions to states with two or more chimneys. For the same value of R_m, transition from one-chimney states to two-chimney states occurred at a large spacing $\lambda_{c,2}$. Although the regime boundary for this transition varies slightly between different runs, we can conclude that $\lambda_{c,2} > 2\lambda_{c,1}$. A more detailed theoretical exploration of these morphological transitions presents an interesting opportunity for future work.

5. Discussion

In many practical contexts it is desirable to predict growth conditions which avoid the formation of chimneys in growing mushy layers. In cells that are sufficiently wide to permit the formation of multiple chimneys, experimental and theoretical models have been applied to infer a critical value R_m^c beyond which the mushy layer mode convection will occur (e.g. Fowler 1985; Worster 1992; Chen, Lu & Yang 1994). However, the cell width λ provides an additional constraint on the existence of convective instability. In particular, Wells *et al.* (2010) studied the evolution of finite amplitude states of convection with chimneys and showed that as λ is decreased the chimneys are extinguished via a saddle-node bifurcation at some critical $\lambda_c(R_m)$. The present work provides the first experimental observation of this finite-sample-size effect on buoyancy-driven convection in the solidification of mushy layers.

We observe a discernible transition of the flow field in the liquid region overlying the mushy layer as mush Rayleigh number R_m and cell width are varied. The flow instability is systematically quantified by the sample width λ and R_m for a variety of liquid concentrations. In figure 6 we showed two sets of data from experiments conducted at two different cooling rates. At a high cooling rate, the resulting value of R_m and the sample width λ (indicated by the upward triangles in figure 7*b*) characterize a stable, no-chimney state (figure 6*a*). A small reduction of the cooling rate increases the value of R_m (shown by the downward triangles in figure 7*b*), and causes a flow instability in the mushy layer that results in a new state dominated by the formation of vigorous chimney plumes in the liquid region (figure 6*b*). Using the same nominal experimental control parameters, the critical Rayleigh number in different runs varies less than 30 %, as is also evident from the data shown in figure 8. Thus, these experimental studies provide reliable results and a general framework for direct comparisons with the prior numerical and theoretical studies, revealing that the system becomes less stable to the onset of flow if either the cell width, Rayleigh number or liquid concentration are increased.

In determining the unknown reference permeability Π_0 of the mushy layer, we compared experimental and numerical results for the instability of the mushy-layer mode of convection summarized in figure 7. Good comparison can be achieved using a single value of the permeability $\Pi_0 = 1.6 \times 10^{-5}$ cm^2 across the entire experimental range of C_0. This suggests that the reference permeability is relatively insensitive to changes in the liquid concentration. It is interesting to compare our estimate of the reference permeability in our quasi-two-dimensional experiment to previous estimates.

https://doi.org/10.1017/jfm.2012.219 Published online by Cambridge University Press

For example, for solidification in a fully three-dimensional experimental cell Tait & Jaupart (1992) estimated a mean permeability value of $\Pi = 8 \times 10^{-4}$ cm^2. In their Appendix B, Tait & Jaupart (1992) compare the Carman–Kozeny relation to a different polynomial form due to Happel & Brenner (1986) in terms of dimensionless functions of porosity, and show that they are comparable with the exception of very high porosity (greater than 0.9). Neufeld & Wettlaufer (2008*a*) estimated a reference permeability $\Pi_0 = 1.75 \times 10^{-3}$ cm^2 by comparing to a linear stability threshold for the onset of shear-enhanced convection. Finally, Chen & Chen (1991) estimated a significantly lower value of the mean permeability $\Pi = 2.4 \times 10^{-5}$ cm^2 based on the Carman–Kozeny relation and solid fractions measured via computed tomography. However, this corresponds to a permeability both after the onset of convection and measured two days after the end of the experiment, allowing the system to evolve away from the initial value of permeability before convective onset. Hence, the difference in magnitude of the inferred reference permeability between our experiments and those of Tait & Jaupart (1992) and Neufeld & Wettlaufer (2008*b*) suggest that the permeability is significantly lower for solidification in a quasi-two-dimensional cell than for a three-dimensional cell.

Through this dynamical constraint of the permeability, the theoretical model for convecting states of finite amplitude successfully captures the form of the observed stability boundary to within the inter-experimental variability of one increment in sample width. This suggests that the theoretical framework of Wells *et al.* (2010) may provide a useful tool in future studies to investigate how chimney formation is influenced by additional factors, such as coupling to flow in the overlying liquid, in a fully nonlinear setting.

Acknowledgements

The authors thank Yale University for support, the referees for their comments and suggestions and S. Toppaladoddi for a helpful reading of the galley proofs. J.S.W. thanks the Wenner-Gren and John Simon Guggenheim Foundations, the Swedish Research Council and the Helmholtz Gemeinschaft Alliance ‘Planetary Evolution and Life’ for support of this research.

REFERENCES

ADAMS, J. C. 1989 MUDPACK: multigrid portable FORTRAN software for the efficient solution of linear elliptic partial differential equations. *Appl. Math. Comput.* **34**, 113–146.

AMBERG, G. & HOMSY, G. M. 1993 Nonlinear analysis of buoyant convection in binary solidification with application to channel formation. *J. Fluid Mech.* **252**, 79–98.

ANDERSON, D. M. & WORSTER, M. G. 1995 Weakly nonlinear analysis of convection in mushy layers during the solidification of binary alloys. *J. Fluid Mech.* **302**, 307–331.

AUSSILLOUS, P., SEDERMAN, A. J., GLADDEN, L. F., HUPPERT, H. E. & WORSTER, M. G. 2006 Magnetic resonance imaging of structure and convection in solidifying mushy layers. *J. Fluid Mech.* **552**, 99–125.

BECKERMANN, C., GU, J. & BOETTINGER, W. 2000 Development of a freckle predictor via Rayleigh number method for single-crystal nickel-base superalloy castings. *Metall. Mater. Trans.* A **31**, 2545–2557.

BERGMAN, M. I. & FEARN, D. R. 1994 Chimneys on the Earth’s inner–outer core boundary? *Geophys. Res. Lett.* **21** (6), 477–480.

BRIGGS, W. L., HENSON, V. E. & MCCORMICK, S. F. 2000 *A Multigrid Tutorial*. SIAM.

CHEN, C. F. & CHEN, F. 1991 Experimental study of directional solidification of aqueous ammonium chloride solution. *J. Fluid Mech.* **227**, 567–586.

https://doi.org/10.1017/jfm.2012.219 Published online by Cambridge University Press

CHEN, F., LU, J. W. & YANG, T. L. 1994 Convective instability in ammonium chloride solution directionally solidified from below. *J. Fluid Mech.* **276**, 163–187.

CHUNG, C. A. & WORSTER, M. G. 2002 Steady-state chimneys in a mushy layer. *J. Fluid Mech.* **455**, 387–411.

COPLEY, S. M., GIAMEI, A. F., JOHNSON, S. M. & HORNBECKER, M. F. 1970 The origin of freckles in unidirectionally solidified castings. *Metall. Trans.* **1** (8), 2193–2204.

FELICELLI, S. D., HEINRICH, J. C. & POIRIER, D. R. 1998 Three-dimensional simulations of freckles in binary alloys. *J. Cryst. Growth* **191**, 879–888.

FELTHAM, D. L., UNTERSTEINER, N., WETTLAUFER, J. S. & WORSTER, M. G. 2006 Sea ice is a mushy layer. *Geophys. Res. Lett.* **33**, L14501.

FOWLER, A. C. 1985 The formation of freckles in binary alloys. *IMA J. Appl. Maths* **35**, 159–174.

GIAMEI, A. F. & KEAR, B. H. 1970 On nature of freckles in nickel base superalloys. *Metall. Trans.* **1**, 2185–2192.

GUBA, P. & WORSTER, M. G. 2006 Nonlinear oscillatory convection in mushy layers. *J. Fluid Mech.* **553**, 419–443.

GUBA, P. & WORSTER, M. G. 2010 Interactions between steady and oscillatory convection in mushy layers. *J. Fluid Mech.* **645**, 411–434.

GUO, J. & BECKERMANN, C. 2003 Three-dimensional simulation of freckle formation during binary alloy solidification: effect of mesh spacing. *Numer. Heat Transfer* A **44** (6), 559–576.

HAPPEL, J. & BRENNER, H. 1986 *Low Reynolds Number Hydrodynamics*. M. Nijhoff.

HEINRICH, J. C. & POIRIER, D. R. 2004 Convection modelling in directional solidification. *C. R. Méc.* **332** (5–6), 429–445.

JAIN, J., KUMAR, A. & DUTTA, P. 2007 Role of plume convection and remelting on the mushy layer structure during directional solidification. *J. Phys.* D **40** (4), 1150–1160.

KATZ, R. F. & WORSTER, M. G. 2008 Simulation of directional solidification, thermochemical convection, and chimney formation in a Hele-Shaw cell. *J. Comput. Phys.* **227** (23), 9823–9840.

KELLER, H. B. 1977 Numerical solution of bifurcation and nonlinear eigenvalue problems. In *Applications of Bifurcation Theory* (ed. P. Rabinowitz), pp. 359–384. Academic.

MULLINS, W. W. & SEKERKA, R. F. 1964 Stability of a planar interface during solidification of a dilute binary alloy. *J. Appl. Phys.* **35** (2), 444–451.

NEUFELD, J. A. & WETTLAUFER, J. S. 2008*a* An experimental study of shear-enhanced convection in a mushy layer. *J. Fluid Mech.* **612**, 363–385.

NEUFELD, J. A. & WETTLAUFER, J. S. 2008*b* Shear-enhanced convection in a mushy layer. *J. Fluid Mech.* **612**, 339–361.

OERTLING, A. B. & WATTS, R. G. 2004 Growth of and brine drainage from NaCl–H_2O freezing: a simulation of young sea ice. *J. Geophys. Res.* **109** (C4), C04013.

PEPPIN, S. S. L., AUSSILLOUS, P., HUPPERT, H. E. & WORSTER, M. G. 2007 Steady-state mushy layers: experiments and theory. *J. Fluid Mech.* **570**, 69–77.

PEPPIN, S. S. L., HUPPERT, H. E. & WORSTER, M. G. 2008 Steady-state solidification of aqueous ammonium chloride. *J. Fluid Mech.* **599**, 465–476.

ROPER, S. M., DAVIS, S. H. & VOORHEES, P. 2007 Convection in a mushy zone forced by sidewall heat losses. *Metall. Mater. Trans.* A **38A**, 1069–1079.

ROPER, S. M., DAVIS, S. H. & VOORHEES, P. 2011 Localisation of convection in mushy layers by weak background flow. *J. Fluid Mech.* **675**, 518–528.

SCHULZE, T. & WORSTER, M. 1998 A numerical investigation of steady convection in mushy layers during the directional solidification of binary alloys. *J. Fluid Mech.* **356**, 199–220.

SCHULZE, T. & WORSTER, M. 2005 A time-dependent formulation of the mushy-zone free-boundary problem. *J. Fluid Mech.* **541**, 193–202.

SOLOMON, T. H. & HARTLEY, R. 1998 Measurements of the temperature field of mushy and liquid regions during solidification of aqueous ammonium chloride. *J. Fluid Mech.* **358**, 87–106.

TAIT, S. & JAUPART, C. 1992 Compositional convection in a reactive crystalline mush and melt differentiation. *J. Geophys. Res.* **97**, 6735–6756.

US NATIONAL RESEARCH COUNCIL, 2003 *International Critical Tables of Numerical Data, Physics, Chemistry, and Technology*.

https://doi.org/10.1017/jfm.2012.219 Published online by Cambridge University Press

WELLS, A. J., WETTLAUFER, J. S. & ORSZAG, S. A. 2010 Maximum potential energy transport: a variational principle for solidification problems. *Phys. Rev. Lett.* **105**, 254502.

WELLS, A. J., WETTLAUFER, J. S. & ORSZAG, S. A. 2011 Brine fluxes from growing sea ice. *Geophys. Res. Lett.* **38**, L04501.

WETTLAUFER, J. S., WORSTER, M. G. & HUPPERT, H. E. 1997*a* Natural convection during solidification of an alloy from above with application to the evolution of sea ice. *J. Fluid Mech.* **344**, 291–316.

WETTLAUFER, J. S., WORSTER, M. G. & HUPPERT, H. E. 1997*b* The phase evolution of young sea ice. *Geophys. Res. Lett.* **24** (10), 1251–1254.

WHITEOAK, S. H., HUPPERT, H. E. & WORSTER, M. G. 2008 Conditions for defect-free solidification of aqueous ammonium chloride in a quasi two-dimensional directional solidification facility. *J. Cryst. Growth* **310** (15), 3545–3551.

WORSTER, M. G. 1992 Instabilities of the liquid and mushy regions during solidification of alloys. *J. Fluid Mech.* **237**, 649–669.

WORSTER, M. G. 1997 Convection in mushy layers. *Annu. Rev. Fluid Mech.* **29**, 91–122.

https://doi.org/10.1017/jfm.2012.219 Published online by Cambridge University Press